

**Orientational dependence of intrinsic orbital and spin Hall effects in hcp structure materials**Hojun Lee <sup>\*</sup>, Byeonghyeon Choi,<sup>\*</sup> and Hyun-Woo Lee <sup>†</sup>*Department of Physics, Pohang University of Science and Technology, Pohang 37673, Korea*

(Received 14 September 2021; revised 9 December 2021; accepted 10 January 2022; published 25 January 2022)

We investigate the orientation dependence of the intrinsic orbital Hall effect (OHE) and spin Hall effect (SHE) in hexagonal close-packed (hcp) structure materials. The symmetry constraints of the hcp structure restrict the orbital (spin) current to the orbital (spin) Hall current. It also shows that there exist three symmetry-wise independent orientations in the hcp structure. We calculate the orbital Hall conductivity (OHC) and the spin Hall conductivity (SHC) of three hcp materials (Sc, Y, and Zr). We find that all these materials have sizable OHC, while the SHC is orders of magnitude smaller. Especially, the OHCs of Sc and Zr have significant orientation dependence, which may be employed to experimentally probe the OHE.

DOI: [10.1103/PhysRevB.105.035142](https://doi.org/10.1103/PhysRevB.105.035142)**I. INTRODUCTION**

The orbital Hall effect (OHE) is a phenomenon where a transverse orbital angular momentum current is generated by an external electric field [1–4]. The OHE was introduced as an analogy of the spin Hall effect (SHE) [5,6] with replacing spin current by orbital angular momentum current. Although Bloch states include both spin and orbital degrees of freedom, unlike spin, orbital angular momentum is usually expected not to play a prominent dynamical role due to orbital quenching [7]. In limited systems, it was argued that an Aharonov-Bohm phase originated from orbitals is the origin of the SHE and that the SHE is related to the OHE [2,8–10]. Orbital-texture-based mechanism, suggested by Go *et al.* [1,11], demonstrated that the OHE can arise in centrosymmetric systems through momentum-space orbital texture and argued that the OHE is responsible for the SHE. In general, the spin-orbit coupling (SOC) is not necessary for the OHE [1,2,11], but it is crucial to convert the OHE into the SHE [1,11]. Recent studies demonstrate that the OHE is closely related also to the valley Hall effect [12,13]. Despite its theoretical importance, experimental detection of the OHE remains challenging since distinguishing it from the SHE is difficult partly because very little is known about properties of an orbital angular momentum current and also because simple symmetry analysis cannot distinguish the OHE from the SHE since they share identical symmetry transformation properties.

This paper investigates theoretically the orientation dependence of the intrinsic OHE and SHE. If the dependence of the OHE differs from the orientation dependence of the SHE, the orientation dependence may be used to distinguish the OHE from the SHE. In crystal structures with high symmetry such as face-centered cubic (fcc) or body-centered cubic (bcc), the orientation dependence is absent, however. We thus examine a crystal structure with lower symmetry: hexagonal

close-packed (hcp) structure (Fig. 1). The hcp structure is common in nature, and about 30 elements crystallize in the hcp structure. As we demonstrate below, the hcp structure has different nonequivalent orientations. For instance, an electric field along the  $\hat{x}$  direction may induce different responses to what an electric field along the  $\hat{z}$  direction may do. This is in contrast to bcc and fcc structures, where such orientation dependence is forbidden due to rich geometric symmetries of the two crystal structures. The orientation dependence in the hcp structure should apply to the OHE and the SHE. If the strength of the OHE differs significantly depending on the orientation of the hcp crystal structure but the strength of the SHE does not, the orientation dependence may be exploited to experimentally probe the OHE.

In this paper, we analyze the orientation dependence of the OHE and the SHE in Sc, Y, and Zr, all of which have the hcp structure. First, we investigate the symmetry constraints in the hcp structure and find that the longitudinal orbital (spin) current is forbidden and only orbital (spin) Hall current is allowed. The symmetry analysis also shows that there exist three symmetry-wise independent orientations. We also verify the symmetry constraints by explicitly calculating the orbital Hall conductivities (OHC) and the spin Hall conductivities (SHC) of the three real hcp structure materials (Sc, Y, and Zr) numerically based on the first principle density functional theory (DFT) calculation. All these materials have sizable OHCs. In particular, the OHCs of Sc and Zr have significant orientation dependence, which may be tested in experiments. We also notice that the SHCs are orders of magnitude smaller for these materials in all orientations. Thus, distinguishing the OHC from the SHC should be viable.

**II. SYMMETRY ANALYSIS**

The orbital angular momentum and the spin angular momentum share the identical symmetry transformation properties. Thus, the symmetry analyses of the OHE and the SHE are identical. To avoid redundancy, we present below the symmetry analysis of the OHE only. To investigate the orientation

<sup>\*</sup>These authors contributed equally to this work.<sup>†</sup>Corresponding author: hwl@postech.ac.kr

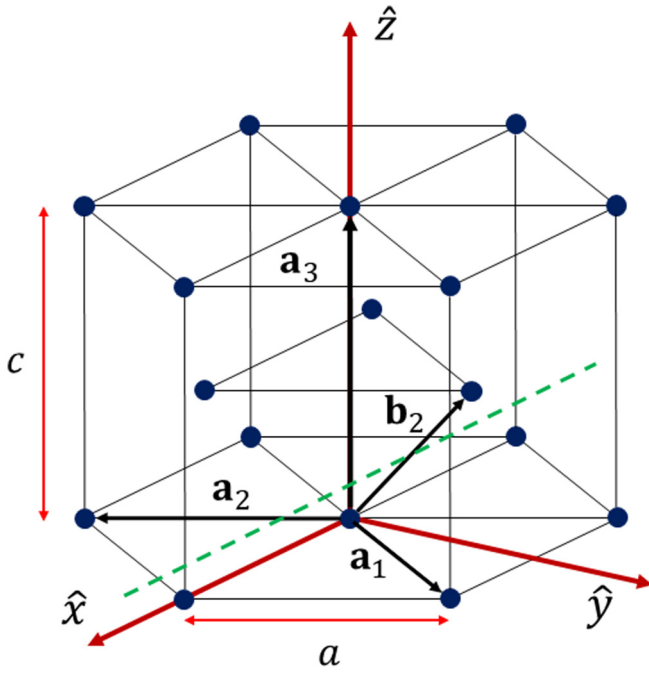


FIG. 1. Illustration of a conventional unit cell of the hcp structure and chosen Cartesian coordinate system. The hcp structure can be described as a hexagonal Bravais lattice with a two-atom basis [14]. The primitive lattice vector in a Cartesian coordinate system can be chosen as  $\mathbf{a}_1 = (\frac{1}{2}a, \frac{\sqrt{3}}{2}a, 0)$ ,  $\mathbf{a}_2 = (\frac{1}{2}a, -\frac{\sqrt{3}}{2}a, 0)$ ,  $\mathbf{a}_3 = (0, 0, c)$ . Then, the basis atoms are given by  $\mathbf{b}_1 = (0, 0, 0)$ ,  $\mathbf{b}_2 = (0, \frac{\sqrt{3}}{3}a, \frac{c}{2})$ . Here,  $a$  and  $c$  are the lattice constants and  $c = \sqrt{\frac{8}{3}}a$  for ideal hcp structure. The green dotted line presents the  $\pi$ -rotation symmetry axis which is parallel to the  $\hat{x}$  axis and passes through the midpoint of  $\mathbf{b}_1$  and  $\mathbf{b}_2$ . Since the symmetry axis is orthogonal to the  $\mathbf{b}_2$  vector, the  $\pi$ -rotation maps  $(0, 0, 0)$  and  $(0, \frac{\sqrt{3}}{3}a, \frac{c}{2})$  to each other.

dependence of the orbital conductivity in the hcp structure, we consider a situation in which the orbital current flows along the  $\alpha$  direction with orbital angular momentum ( $\mathbf{L}$ ) in the  $\beta$  direction due to the electric field ( $\mathbf{E}$ ) in the  $\gamma$  direction. We define the orbital current  $j_{\alpha\beta}$  as

$$j_{\alpha\beta} = \frac{\langle L_{\beta} v_{\alpha} + v_{\alpha} L_{\beta} \rangle}{2} \quad (1a)$$

and examine its linear response to  $\mathbf{E}$ ,

$$j_{\alpha\beta} = \sigma_{\alpha\beta\gamma} E_{\gamma}. \quad (1b)$$

Here  $L_{\beta}$  is the  $\beta$  component of the orbital angular momentum,  $v_{\alpha}$  is the  $\alpha$  component of the velocity operator, and  $\sigma_{\alpha\beta\gamma}$  is the orbital conductivity for this situation. We set each direction to follow one of the Cartesian coordinate system basis  $\hat{x}$ ,  $\hat{y}$ ,  $\hat{z}$ , defined in Fig. 1. Any other directions can be expressed as their linear combination. Then, we get 27  $(\alpha, \beta, \gamma)$  combinations for the orbital conductivity  $\sigma_{\alpha\beta\gamma}$ . A large portion of them is forced to vanish by the symmetry of the hcp structure. Moreover, nonvanishing combinations are mutually related to each other so that there exist a small number of independent nonvanishing combinations, as demonstrated below.

The space group of the hcp structure is  $P6_3/mmc$ . It has one horizontal mirror plane, one sixfold rotation axis ( $6_3$ ),

six vertical mirror planes, one inversion center, one threefold rotation axis, and six twofold rotation axes. The important symmetries to identify the possible  $(\alpha, \beta, \gamma)$  combinations are the mirror symmetry about the  $xy$  plane, the mirror symmetry about the  $yz$  plane, and the  $\pi$ -rotation symmetry about the axis which is parallel to the  $\hat{x}$  axis and passes through the midpoint of  $\mathbf{b}_1$  and  $\mathbf{b}_2$  (green dotted line in Fig. 1). Due to these symmetries,  $\sigma_{\alpha\beta\gamma} = 0$  if any two indices of  $(\alpha, \beta, \gamma)$  combination are the same. Thus, all three indices should be different, implying that the longitudinal orbital current is forbidden and only the orbital Hall current is allowed. This constraint can be understood as follows. For example, suppose that  $(\hat{y}, \hat{x}, \hat{x})$  combination is physically possible, which means that there exists a nonzero orbital current flowing along the  $\hat{y}$  direction with  $\mathbf{L}$  in the  $\hat{x}$  direction due to the  $\mathbf{E}$  in the  $\hat{x}$  direction. The mirror symmetry about the  $xy$  plane implies that the lattice structure is invariant under the transformation of  $\hat{z} \rightarrow \hat{z}' = -\hat{z}$ . This mirror transforms  $(\hat{y}, \hat{x}, \hat{x})$  to  $(\hat{y}, -\hat{x}, \hat{x})$ , which means that there exists nonzero current flowing along the  $\hat{y}$  direction with  $\mathbf{L}$  in the  $-\hat{x}$  direction due to the  $\mathbf{E}$  in the  $\hat{x}$  direction. However, it is contradiction to the initial assumption. Therefore,  $(\hat{y}, \hat{x}, \hat{x})$  combination should be physically impossible. In a similar way, all other combinations with any indices identical are forbidden by the symmetries of the hcp structure.

The symmetries of the hcp structure not only restrict the number of the possible  $(\alpha, \beta, \gamma)$  combinations, but also relate the nonvanishing combinations with each other. For example, consider  $\sigma_{yzx}$ . Equation (1) implies that  $\sigma_{yzx}$  is determined by  $\langle L_z v_y + v_y L_z \rangle / 2$ . Since the hcp structure has threefold rotation axis parallel to the  $\hat{z}$  axis, the lattice structure is invariant under the  $2\pi/3$  rotation and the  $4\pi/3$  rotation around this axis. Invariance under the  $2\pi/3$  rotation means that  $\sigma_{yzx}$  is invariant under the rotation transformation of  $\hat{x} \rightarrow \hat{x}' = -\frac{1}{2}\hat{x} + \frac{\sqrt{3}}{2}\hat{y}$ ,  $\hat{y} \rightarrow \hat{y}' = -\frac{\sqrt{3}}{2}\hat{x} - \frac{1}{2}\hat{y}$ , and  $\hat{z} \rightarrow \hat{z}' = \hat{z}$ . By applying this to Eq. (1), the orbital current  $j_{y'z'}$ , corresponding to  $\sigma_{y'z'x'}$ , satisfies that  $j_{y'z'} = \sigma_{y'z'x'} E_{x'}$ . The orbital current  $j_{y'z'}$  can be represented as  $j_{y'z'} = -\frac{\sqrt{3}}{2}j_{xz} - \frac{1}{2}j_{yz}$ , and the electric field  $E_{x'}$  can be represented as  $E_{x'} = -\frac{1}{2}E_x + \frac{\sqrt{3}}{2}E_y$ . Thus, considering that  $\sigma_{xzx} = \sigma_{yzy} = 0$  and  $j_{xz} = \sigma_{xzy} E_y$ ,  $j_{yz} = \sigma_{yzx} E_x$ , we obtain  $\sigma_{xzy} = -\sigma_{yzx}$ . In a similar way, by considering the  $2\pi/3$  rotation and the  $4\pi/3$  rotation, the relations  $\sigma_{xyz} = -\sigma_{yxz}$  and  $\sigma_{zyx} = -\sigma_{zxy}$  are obtained. That is, the interchange of  $x$  and  $y$  indices reverses the sign of the OHC. However, we emphasize that the interchange of  $z$  and  $x$ , and the interchange of  $z$  and  $y$  do not result in symmetry-enforced relations. Thus, the hcp structure has three independent OHCs:  $\sigma_{xyz} = -\sigma_{yxz}$ ,  $\sigma_{yzx} = -\sigma_{xzy}$  and  $\sigma_{zxy} = -\sigma_{zyx}$ .

### III. CALCULATION

#### A. Computational details

The full-potential DFT calculation proceeds as follows. In the first step, we obtained the electronic structures of all materials using the full-potential linearization augmented plane wave method [15] from the code FLEUR [16]. The band structures of the materials (Sc, Y, and Zr) are presented in Fig. 2. We used Perdew-Burke-Ernzerhof

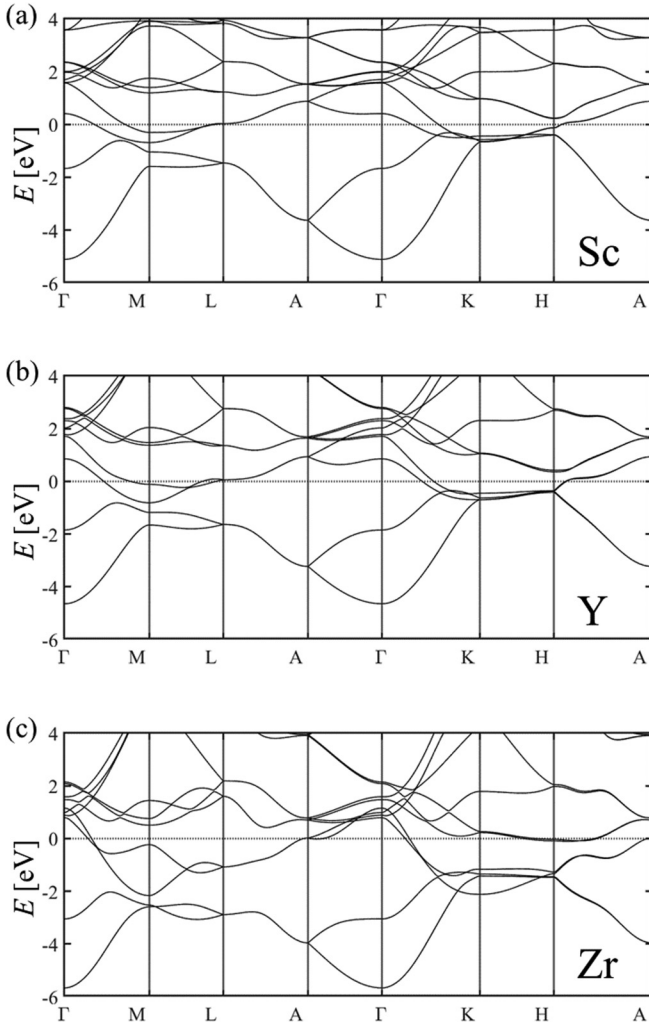


FIG. 2. Band structures of hcp (a) Sc, (b) Y, and (c) Zr obtained from the full-potential DFT calculation. Horizontal dotted lines present the Fermi energy.

exchange-correlation functional within the generalized gradient approximation [17]. For the lattice constants of each structure, values in Refs. [18,19] were used. The muffin-tin radii of each atom and the plane wave cutoffs were commonly set to  $2.3 a_0$  and  $5.0 a_0^{-1}$ , respectively, where  $a_0$  is the Bohr radius. For the Brillouin zone samplings, the  $16 \times 16 \times 16$  Monkhorst-Pack  $\mathbf{k}$  mesh was used [20]. The second variation scheme was used to include the SOC.

In the second step, the maximally localized Wannier functions (MLWFs) were obtained from the Bloch states with the code WANNIER90 [21]. For the Brillouin zone samplings, the equidistant  $8 \times 8 \times 8$   $\mathbf{k}$ -mesh which includes the gamma point was used. The initial projections of the Bloch states were chosen as  $s$ ,  $p_x$ ,  $p_y$ ,  $p_z$ ,  $d_{xy}$ ,  $d_{yz}$ ,  $d_{zx}$ ,  $d_{x^2-y^2}$ , and  $d_{z^2}$ . For each structure, we obtained a total of 36 MLWFs, 18 per atom out of 72 bands. The frozen windows were set to include a region 8 eV higher than the Fermi energy. Also, the Hamiltonian spin, orbital angular momentum and position operators were transformed in the basis of MLWFs to construct the tight-binding model.

## B. Kubo formula

To evaluate OHC ( $\sigma_{\text{OH}}$ ) and SHC ( $\sigma_{\text{SH}}$ ), we employ the Kubo formula within the linear response theory:

$$\sigma_{\text{OH(SH)}} = \frac{e}{\hbar} \sum_{n \neq m} \int \frac{d^3 k}{(2\pi)^3} (f_{m\mathbf{k}} - f_{n\mathbf{k}}) \Omega_{nm\mathbf{k}}^{X_\beta}, \quad (2a)$$

$$\Omega_{nm\mathbf{k}}^{X_\beta} = \hbar^2 \text{Im} \left( \frac{\langle u_{n\mathbf{k}} | j_\alpha^{X_\beta} | u_{m\mathbf{k}} \rangle \langle u_{m\mathbf{k}} | v_\gamma | u_{n\mathbf{k}} \rangle}{(E_{n\mathbf{k}} - E_{m\mathbf{k}} + i\eta)^2} \right), \quad (2b)$$

where  $f_{n\mathbf{k}}$  is the Fermi-Dirac distribution function,  $v_\gamma$  is  $\gamma$  component of the velocity operator,  $j_\alpha^{X_\beta} = (X_\beta v_\alpha + v_\alpha X_\beta)/2$  is the conventional orbital (spin) current operator corresponding to the orbital (spin) current flowing along the  $\alpha$  direction with  $\beta$  component of the orbital (spin) angular momentum  $X_\beta = L_\beta (S_\beta)$ ,  $|u_{n,\mathbf{k}}\rangle$  is a periodic part of the Bloch state of the Hamiltonian, and  $E_{n\mathbf{k}}$  is the corresponding energy eigenvalue. It is natural that the orbital angular momentum is defined around the atomic center when the Kubo formula [Eq. (2)] is employed to calculate the OHC for a structure with one atom in a unit cell. The  $\mathbf{k}$ -space integration in Eq. (2a) was made on a uniform  $120 \times 120 \times 120$   $\mathbf{k}$  mesh. We set  $\eta$  in Eq. (2b) to 25 meV. The resultant OHCs and SHCs in Figs. 2–4 were calculated by increasing the Fermi energy ( $E_F$ ) from  $-1.0$  eV to  $1.0$  eV with 0.04 eV steps (the actual Fermi energy is 0 eV in Figs. 3, 4, 5).

We can use the Kubo formula in Eq. (2) to confirm the relation between OHCs in different orientations predicted above. In Eq. (2), only the numerator of  $\Omega_{nm\mathbf{k}}^{X_\beta}$ ,  $\langle u_{n\mathbf{k}} | j_\alpha^{X_\beta} | u_{m\mathbf{k}} \rangle \langle u_{m\mathbf{k}} | v_\gamma | u_{n\mathbf{k}} \rangle$ , depends on the orientation. So, we can test the relation between OHCs in different orientations by analyzing the numerator. For example, we can verify  $\sigma_{xzy} = -\sigma_{yzx}$  from Eq. (2) by considering the  $2\pi/3$ -rotation and  $4\pi/3$ -rotation symmetry about the threefold rotation axis parallel to the  $\hat{z}$  axis. The numerator of  $\Omega_{nm\mathbf{k}}^{X_z}$  for  $\sigma_{yzx}$ , is  $\langle u_{n\mathbf{k}} | j_y^{X_z} | u_{m\mathbf{k}} \rangle \langle u_{m\mathbf{k}} | v_x | u_{n\mathbf{k}} \rangle$ . From the invariance of the hcp lattice structure under the  $2\pi/3$ -rotation transformation, we obtain

$$\begin{aligned} & \langle u_{n\mathbf{k}} | j_y^{X_z} | u_{m\mathbf{k}} \rangle \langle u_{m\mathbf{k}} | v_x | u_{n\mathbf{k}} \rangle \\ &= \langle u_{n\mathbf{k}} | j_{y'}^{X_{z'}} | u_{m\mathbf{k}} \rangle \langle u_{m\mathbf{k}} | v_{x'} | u_{n\mathbf{k}} \rangle. \end{aligned} \quad (3)$$

Together with the relations  $\hat{x}' = -\frac{1}{2}\hat{x} + \frac{\sqrt{3}}{2}\hat{y}$ ,  $\hat{y}' = -\frac{\sqrt{3}}{2}\hat{x} - \frac{1}{2}\hat{y}$ , and  $\hat{z}' = \hat{z}$ , we obtain from Eq. (3) the relation

$$\sigma_{yzx} = \frac{\sqrt{3}}{4}\sigma_{xzx} - \frac{3}{4}\sigma_{xzy} - \frac{\sqrt{3}}{4}\sigma_{zyy} + \frac{1}{4}\sigma_{yzx}. \quad (4)$$

From the invariance of the hcp lattice structure under the  $4\pi/3$ -rotation transformation, we obtain

$$\begin{aligned} & \langle u_{n\mathbf{k}} | j_y^{X_z} | u_{m\mathbf{k}} \rangle \langle u_{m\mathbf{k}} | v_x | u_{n\mathbf{k}} \rangle \\ &= \langle u_{n\mathbf{k}} | j_{y''}^{X_{z''}} | u_{m\mathbf{k}} \rangle \langle u_{m\mathbf{k}} | v_{x''} | u_{n\mathbf{k}} \rangle. \end{aligned} \quad (5)$$

Together with the relations  $\hat{x}' = -\frac{1}{2}\hat{x} - \frac{\sqrt{3}}{2}\hat{y}$ ,  $\hat{y}' = \frac{\sqrt{3}}{2}\hat{x} - \frac{1}{2}\hat{y}$ , and  $\hat{z}' = \hat{z}$ , we obtain from Eq. (5) the relation

$$\sigma_{yzx} = -\frac{\sqrt{3}}{4}\sigma_{xzx} - \frac{3}{4}\sigma_{xzy} + \frac{\sqrt{3}}{4}\sigma_{zyy} + \frac{1}{4}\sigma_{yzx}. \quad (6)$$

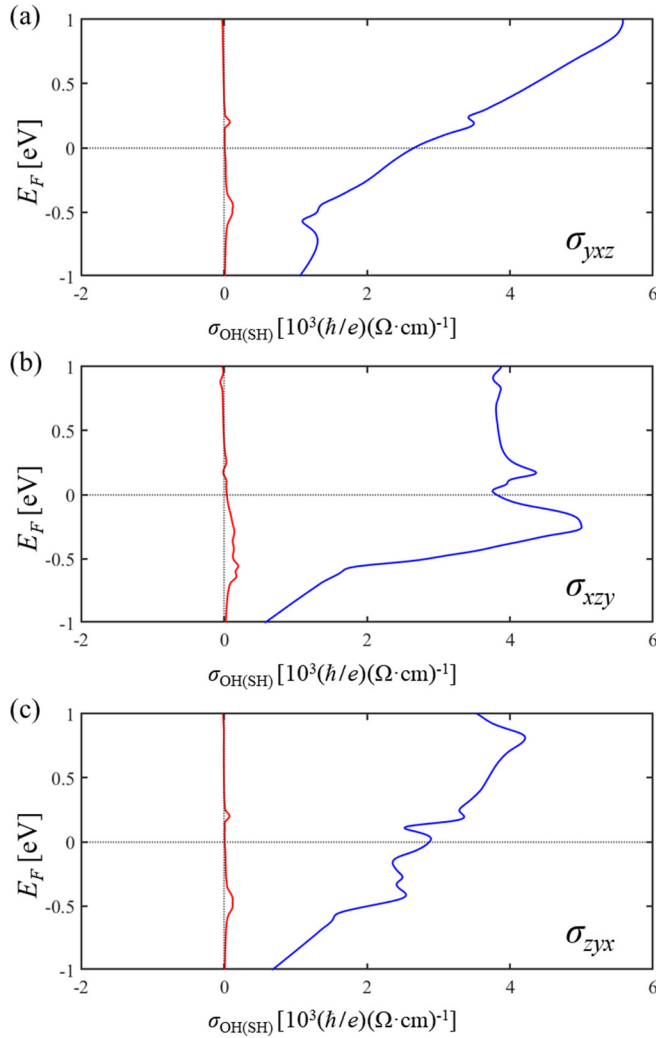


FIG. 3. The Fermi energy ( $E_F$ ) dependence of OHC ( $\sigma_{OH}$ ) (blue line) and SHC ( $\sigma_{SH}$ ) (red line) calculated by the full-potential DFT calculation in Sc. The directions of the orbital (spin) flow ( $\mathbf{v}$ ), orbital (spin) angular momentum ( $\mathbf{L}$  or  $\mathbf{S}$ ), and the electric field ( $\mathbf{E}$ ) are set to be along the (a)  $\hat{y}$ ,  $\hat{x}$ ,  $\hat{z}$ , (b)  $\hat{x}$ ,  $\hat{z}$ ,  $\hat{y}$ , (c)  $\hat{z}$ ,  $\hat{y}$ ,  $\hat{x}$  axis, respectively.

By combining Eq. (4) with Eq. (6), we can verify  $\sigma_{xzy} = -\sigma_{yzx}$ . In a similar way, we can also verify  $\sigma_{xyx} = -\sigma_{yxz}$  and  $\sigma_{zyx} = -\sigma_{zxy}$  by checking  $\langle u_{nk} | J_x^{X_y} | u_{mk} \rangle \langle u_{mk} | v_z | u_{nk} \rangle$  and  $\langle u_{nk} | J_z^{X_y} | u_{mk} \rangle \langle u_{mk} | v_x | u_{nk} \rangle$ , respectively.

The orientation dependence of the OHC of the hcp structure, resulting from its symmetry, is confirmed from the explicit calculation results of the Kubo formula. We present the calculated OHC (blue line) for real hcp structure materials (Sc, Y and Zr) in Figs. 3, 4, 5. The results of SHC (red line), calculated by Eq. (2), are presented together with the OHC results. Horizontal dotted lines present the real Fermi energy ( $E_F = 0$  in Figs. 3, 4, 5). We have verified that our prediction about the orientation dependence of the OHC of the hcp structure is valid for the real hcp structure materials from the results exactly. Thus, we only present the results of the three independent OHCs and SHCs:  $\sigma_{yxz}$ ,  $\sigma_{xzy}$  and  $\sigma_{zyx}$  in Figs. 3, 4, 5.

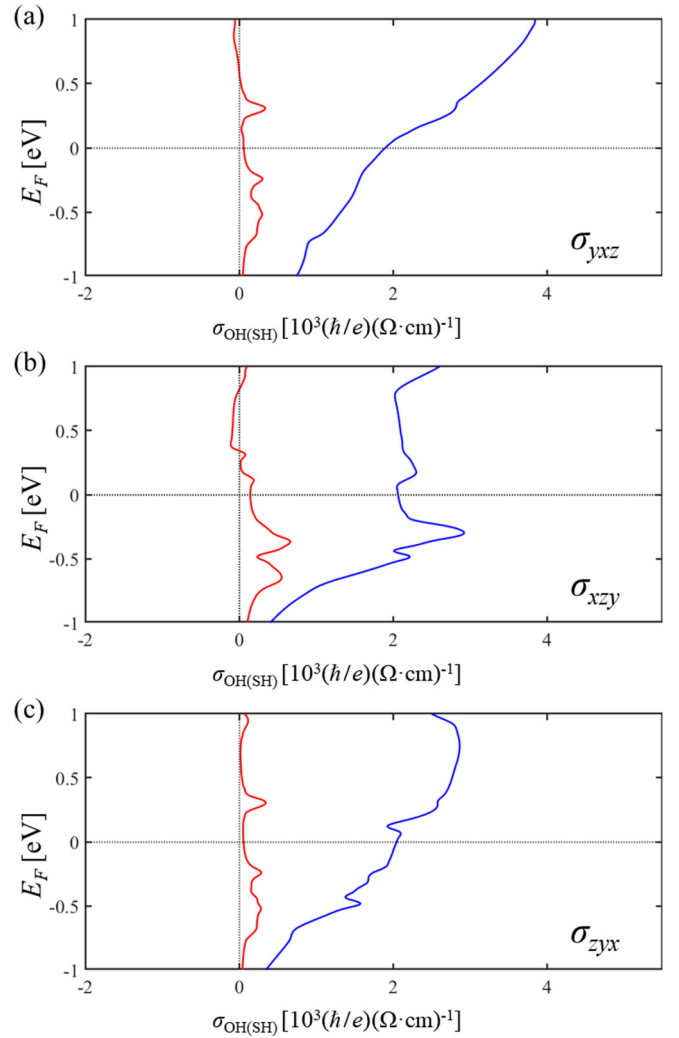


FIG. 4. The Fermi energy ( $E_F$ ) dependence of OHC ( $\sigma_{OH}$ ) (blue line) and SHC ( $\sigma_{SH}$ ) (red line) calculated by the full-potential DFT calculation in Y. The directions of the orbital (spin) flow ( $\mathbf{v}$ ), orbital (spin) angular momentum ( $\mathbf{L}$  or  $\mathbf{S}$ ), and the electric field ( $\mathbf{E}$ ) are set to be along the (a)  $\hat{y}$ ,  $\hat{x}$ ,  $\hat{z}$ , (b)  $\hat{x}$ ,  $\hat{z}$ ,  $\hat{y}$ , (c)  $\hat{z}$ ,  $\hat{y}$ ,  $\hat{x}$  axis, respectively.

#### IV. DISCUSSION

Since the OHCs are sizable for any directions near the real Fermi energy in Sc, Y, and Zr, the results we obtained may be measured in experiment. Especially, the OHC of Zr has significant orientation dependence (Fig. 5):  $\sigma_{OH,yxz} \approx 6540$ ,  $\sigma_{OH,xzy} \approx 2880$ , and  $\sigma_{OH,zyx} \approx 4350$  ( $\hbar/e$ )( $\Omega \text{ cm}$ ) $^{-1}$ . Thus, we expect that the differences between  $\sigma_{OH,yxz}$ ,  $\sigma_{OH,xzy}$  and  $\sigma_{OH,zyx}$  may be tested in experiments. The OHC of Sc also has orientation dependence (Fig. 3):  $\sigma_{OH,yxz} \approx 2660$ ,  $\sigma_{OH,xzy} \approx 3810$ , and  $\sigma_{OH,zyx} \approx 2880$  ( $\hbar/e$ )( $\Omega \text{ cm}$ ) $^{-1}$ . In the case of Sc, the orientation dependence of the OHC is smaller than the case of Zr, but the difference between  $\sigma_{OH,xzy}$  and  $\sigma_{OH,yxz}$  (or  $\sigma_{OH,zyx}$ ) is significant. Thus, we expect that the difference can be tested in experiments. In the case of Y, the orientation dependence of the OHC is weak (Fig. 4):  $\sigma_{OH,yxz} \approx 1900$ ,  $\sigma_{OH,xzy} \approx 2060$ , and  $\sigma_{OH,zyx} \approx 2050$  ( $\hbar/e$ )( $\Omega \text{ cm}$ ) $^{-1}$ .

In Sc, Y and Zr, the SHCs are much smaller than the OHCs in all orientations, which is natural since all these elements

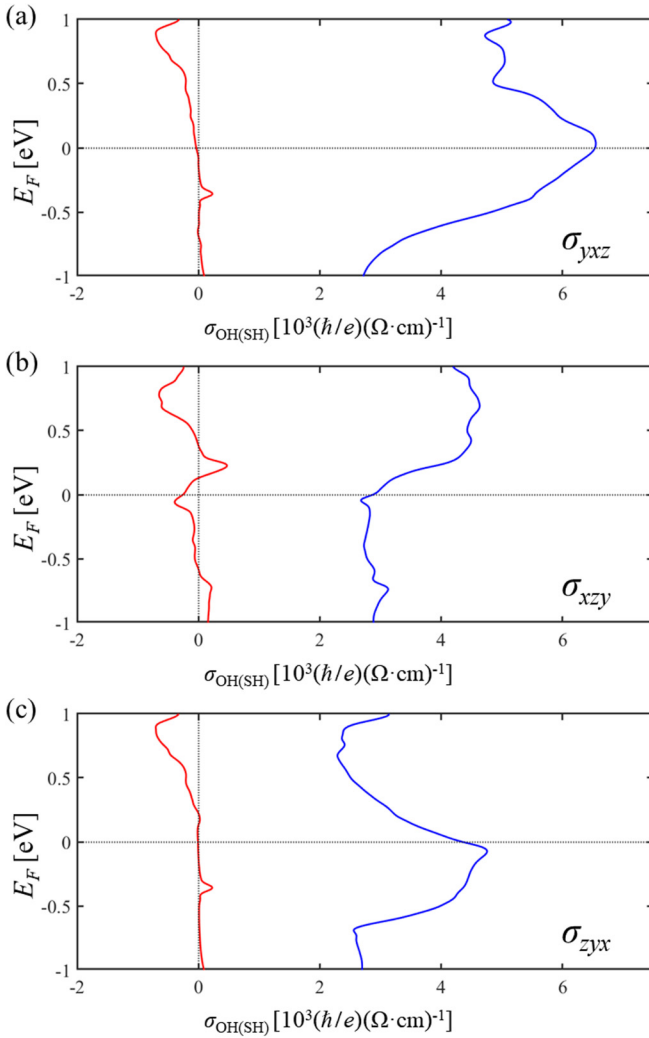


FIG. 5. The Fermi energy ( $E_F$ ) dependence of OHC ( $\sigma_{OH}$ ) (blue line) and SHC ( $\sigma_{SH}$ ) (red line) calculated by the full-potential DFT calculation in Zr. The directions of the orbital (spin) flow ( $\mathbf{v}$ ), orbital (spin) angular momentum ( $\mathbf{L}$  or  $\mathbf{S}$ ), and the electric field ( $\mathbf{E}$ ) are set to be along the (a)  $\hat{y}$ ,  $\hat{x}$ ,  $\hat{z}$ , (b)  $\hat{x}$ ,  $\hat{z}$ ,  $\hat{y}$ , (c)  $\hat{z}$ ,  $\hat{y}$ ,  $\hat{x}$  axis, respectively.

have the weak SOC. Thus distinguishing the OHC from the SHC should be viable in these materials.

Recently, as the dynamical role of the orbital current has been refocused, a few experiments [22,23] attempted to confirm the existence of the orbital current. For this, the experiments resorted to the orbital torque, the phenomenon in which the orbital current injected into a ferromagnet is converted to spin through the SOC of the ferromagnet and exerts torque to the magnetization of the ferromagnet [24]. The two experiments [25,26] attributed the measured torque to the orbital torque. A recent experiment [27] reported a sizable torque in Zr-based heterostructures and argued that it may be due to the orbital torque. However, the orientation dependence is not examined. We propose that an evidence for

the existence of the orbital current can be added by testing the orientation dependence of the OHE and the SHE in these four hcp materials.

The orientation dependence of the OHE and the SHE in the hcp structure can be applied to other crystal structures, whose symmetry properties contain the important symmetries deriving the symmetry constraints on the OHE and the SHE in the hcp structure. For example, the symmetries of the double hcp structure produce the same constraints as the symmetries of the hcp structure. In the double hcp structure, the mirror symmetry about the  $xy$  plane, the mirror symmetry about the  $yz$  plane, and the  $\pi$ -rotation symmetry about the  $\hat{x}$  axis forbid the longitudinal orbital current and allow only the orbital Hall current. Furthermore, threefold rotation symmetry about the  $\hat{z}$  axis provides the relationship between the OHCs for different orientations, which is the same as the hcp structure.

Lastly we note that our calculation [Eq. (2)] of the OHCs and SHCs takes into account only the Fermi sea contribution and neglects the Fermi surface contribution. Our neglect of the Fermi surface contribution is motivated by Ref. [9], which reports that in the  $4d$  and  $5d$  transition metals, the Fermi sea distribution to the SHC governs the total contribution to the SHC in the weak disorder regime. We assume in this paper that the situation is similar for the OHCs of the materials examined in this paper. Further study on the Fermi surface contribution to the OHCs is necessary, which however goes beyond the scope of this paper.

## V. CONCLUSION

To conclude, we have investigated the orientation dependence of the intrinsic OHE and SHE in the hcp structure. We first examined the symmetry constraints. The symmetries of the hcp structure forbid the longitudinal orbital (spin) current and only allow the OHC and SHC. They not only restrict the types of possible orbital (spin) conductivity, but also relate the possible combinations with each other. We have shown that the hcp structure has three independent OHCs (SHCs):  $\sigma_{xzy} = -\sigma_{yzx}$ ,  $\sigma_{xyz} = -\sigma_{yxz}$ , and  $\sigma_{zyx} = -\sigma_{zxy}$ . We have also calculated the OHCs and the SHCs in the three real hcp materials (Sc, Y, and Zr), and verified the symmetry constraints explicitly. In Sc, Y, and Zr, the OHCs are sizable, while the SHCs are orders of magnitude smaller than the OHCs in all orientations. Thus, distinguishing the OHE from the SHE should be viable in these three materials. In Sc and Zr, especially, the orientation dependence of the OHCs are sizable near the real Fermi energy. Therefore, the orientation dependence of OHCs in these materials may be measured in experiment.

## ACKNOWLEDGMENTS

We thank I. Baek and D. Jo for fruitful discussions. They also helped with crosschecking of numerical calculations. H.-W.L. was supported by the Samsung Science and Technology Foundation (Grant No. BA-1501-51)

- [1] D. Go, D. Jo, C. Kim, and H.-W. Lee, Intrinsic Spin and Orbital Hall Effects from Orbital Texture, *Phys. Rev. Lett.* **121**, 086602 (2018).
- [2] H. Kontani, T. Tanaka, D. S. Hirashima, K. Yamada, and J. Inoue, Giant Orbital Hall Effect in Transition Metals: Origin of Large Spin and Anomalous Hall Effects, *Phys. Rev. Lett.* **102**, 016601 (2009).
- [3] B. A. Bernevig, T. L. Hughes, and S.-C. Zhang, Orbitronics: The Intrinsic Orbital Current in *p*-Doped Silicon, *Phys. Rev. Lett.* **95**, 066601 (2005).
- [4] D. Go, D. Jo, H.-W. Lee, M. Kläui, and Y. Mokrousov, Orbitronics: Orbital currents in solids, *Europhysics Lett.* **135**, 37001 (2021).
- [5] J. Sinova, S. O. Valenzuela, J. Wunderlich, C. H. Back, and T. Jungwirth, Spin Hall effects, *Rev. Mod. Phys.* **87**, 1213 (2015).
- [6] J. E. Hirsch, Spin Hall Effect, *Phys. Rev. Lett.* **83**, 1834 (1999).
- [7] C. Kittel, *Introduction to Solid State Physics, 8th edition* (Wiley & Sons, New York, 2004).
- [8] T. Tanaka and H. Kontani, Intrinsic spin and orbital Hall effects in heavy-fermion systems, *Phys. Rev. B* **81**, 224401 (2010).
- [9] T. Tanaka, H. Kontani, M. Naito, T. Naito, D. S. Hirashima, K. Yamada, and J. Inoue, Intrinsic spin Hall effect and orbital Hall effect in *4d* and *5d* transition metals, *Phys. Rev. B* **77**, 165117 (2008).
- [10] H. Kontani, T. Tanaka, D. S. Hirashima, K. Yamada, and J. Inoue, Giant Intrinsic Spin and Orbital Hall Effects in  $Sr_2MO_4$  ( $M = Ru, Rh, Mo$ ), *Phys. Rev. Lett.* **100**, 096601 (2008).
- [11] D. Jo, D. Go, and H.-W. Lee, Gigantic intrinsic orbital Hall effects in weakly spin-orbit coupled metals, *Phys. Rev. B* **98**, 214405 (2018).
- [12] T. P. Cysne, M. Costa, L. M. Canonico, M. B. Nardelli, R. B. Muniz, and T. G. Rappoport, Disentangling Orbital and Valley Hall Effects in Bilayers of Transition Metal Dichalcogenides, *Phys. Rev. Lett.* **126**, 056601 (2021).
- [13] S. Bhowal and G. Vignale, Orbital Hall effect as an alternative to valley Hall effect in gapped graphene, *Phys. Rev. B* **103**, 195309 (2021).
- [14] M. Miasek, Tight-binding method for hexagonal close-packed structure, *Phys. Rev.* **107**, 92 (1957).
- [15] E. Wimmer, H. Krakauer, M. Weinert, and A. J. Freeman, Full-potential self-consistent linearized-augmented-plane-wave method for calculating the electronic structure of molecules and surfaces:  $O_2$  molecule, *Phys. Rev. B* **24**, 864 (1981).
- [16] <http://www.flapw.de>.
- [17] J. P. Perdew, K. Burke, and M. Ernzerhof, Generalized Gradient Approximation Made Simple, *Phys. Rev. Lett.* **77**, 3865 (1996).
- [18] F. H. Spedding, A. H. Daane, and K. W. Herrmann, The crystal structures and lattice parameters of high-purity scandium, yttrium and the rare earth metals, *Acta Crystallogr.* **9**, 559 (1956).
- [19] B. Olinger and J. C. Jamieson, Zirconium: Phases and compressibility to 120 kilobars, *High Temp.-High Press.* **5**, 123 (1973).
- [20] H. J. Monkhorst and J. D. Pack, Special points for Brillouin-zone integrations, *Phys. Rev. B* **13**, 5188 (1976).
- [21] G. Pizzi *et al.*, Wannier90 as a community code: new features and applications, *J. Phys.: Condens. Matter* **32**, 165902 (2020).
- [22] D. Lee, D. Go, H.-J. Park, W. Jeong, H.-W. Ko, D. Yun, D. Jo, S. Lee, G. Go, J. H. Oh, K.-J. Kim, B.-G. Park, B.-C. Min, H. C. Koo, H.-W. Lee, O. Lee, and K.-J. Lee, Orbital torque in magnetic bilayers, *Nat. Commun.* **12**, 6710 (2021).
- [23] S. Ding, Z. Liang, D. Go, C. Yun, M. Xue, Z. Liu, S. Becker, W. Yang, H. Du, C. Wang, Y. Yang, G. Jakob, M. Kläui, Y. Mokrousov, and J. Yang, Observation of the orbital rashbaedelstein magnetoresistance, [arXiv:2105.04495v2](https://arxiv.org/abs/2105.04495v2) [Phys. Rev. Lett. (to be published)].
- [24] D. Go and H.-W. Lee, Orbital torque: Torque generation by orbital current injection, *Phys. Rev. Research* **2**, 013177 (2020).
- [25] S. Ding, A. Ross, D. Go, L. Baldrati, Z. Ren, F. Freimuth, S. Becker, F. Kammerbauer, J. Yang, G. Jakob, Y. Mokrousov, and M. Kläui, Harnessing Orbital-to-Spin Conversion of Interfacial Orbital Currents for Efficient Spin-Orbit Torques, *Phys. Rev. Lett.* **125**, 177201 (2020).
- [26] J. Kim, D. Go, H. Tsai, D. Jo, K. Kondou, H.-W. Lee, and Y. Otani, Nontrivial torque generation by orbital angular momentum injection in ferromagnetic-metal/Cu/ $Al_2O_3$  trilayers, *Phys. Rev. B* **103**, L020407 (2021).
- [27] Z. C. Zheng, Q. X. Guo, D. Jo, D. Go, L. H. Wang, H. C. Chen, W. Yin, X. M. Wang, G. H. Yu, W. He, H.-W. Lee, J. Teng, and T. Zhu, Magnetization switching driven by current-induced torque from weakly spin-orbit coupled Zr, *Phys. Rev. Research* **2**, 013127 (2020).